



In situ photocalorimetry: An alternative approach to study photocatalysis by tracing heat changes and kinetics

Xingxing Li^a, Zaiyin Huang^{a,b,*}, Zuojiao Liu^a, Kaisheng Diao^a, Gaochao Fan^a, Zhan Huang^a, Xuecai Tan^{a,b}

^a College of Chemistry and Chemical Engineering, Guangxi University for Nationalities, Nanning, 530006, China

^b Key Laboratory of Forest Chemistry and Engineering, Guangxi University for Nationalities, Nanning, 530006, China



ARTICLE INFO

Article history:

Received 11 March 2015

Received in revised form 17 July 2015

Accepted 21 July 2015

Available online 26 July 2015

Keywords:

In situ photocalorimetry

Photocatalysis

Thermodynamics

Ag@AgCl

Photocatalytic mechanism

ABSTRACT

Much effort has been expended recently to investigate photocatalytic mechanisms by in situ spectroscopy. We introduced an alternative method to study photocatalysis thermodynamically by tracing thermodynamics and kinetics in real-time using a light-emitting diode photocalorimeter that includes a commercial microcalorimeter and fiber optics. We were almost able to adjust its baseline to zero by tuning the incident light intensity. After calibration, we used the photocalorimeter to trace heat changes and kinetics in the photocatalysis of methylene blue over a visible-light-driven Ag@AgCl photocatalyst. Three main heat changes occurred: (i) photoresponse of methylene blue molecules and photocatalyst, (ii) balance between endothermic photoresponse and pollutant photodegradation, and (iii) stable exothermic stage in pollutant photodegradation. The photocalorimeter underwent an initial endothermic reaction and a subsequent exothermic stage, and finally maintained a stable exothermic rate of $-(0.1543 \pm 0.0446) \text{ mJ s}^{-1}$ with a pseudo-zero-order process. The heat effects of stages (i), (ii), and (iii) are 73.8, 143.9, and -1939.2 mJ , respectively. The photocatalytic mechanism was discussed in detail. Results from this study are critical to the development of promising applications in in situ photochemistry, physics, and biomedicine.

© 2015 Elsevier B.V. All rights reserved.

1. Introduction

Over the past 30 years, various semiconductors, typically represented by TiO_2 [1] have attracted much attention because of their potential promising application in hydrogen evolution by water splitting [2], organic synthesis [3], and water treatment [4,5]. However, an understanding of the catalytic mechanism and relevant theoretical research has lagged behind, and the lack of clear fundamental theories has led to knowledge in this area being compared to an unknown black box [6]. Owing to limitations of the existing approaches, a novel method or instrument is required to investigate in situ photocatalysis.

Photocalorimetry provides an alternative approach to study in situ photoreaction processes, and allows for the real-time synchronous collection of detailed heat changes and kinetics data during irradiation [7,8]. Traditional methods to investigate photoreaction processes, such as using the ultraviolet (UV)–visible

(vis) spectrum for the determination of degradation rate and high-performance liquid chromatography/high-performance gas chromatography–mass spectrometry for intermediate products analysis, require the irradiation of samples separate from quantitative analytical instruments. However, photocalorimetry takes advantage of the measurement of heat changes with simultaneous sample irradiation [9–11]. The principle of photocalorimetry was introduced in 1939 to determine the quantum efficiency of photosynthesis in algae [12]. Its development can be divided into three stages. The first stage requires the development of a simple thermostatic water bath or a vacuum-jacketed cell equipped with a flat quartz window that admits incident light [12–17]. The second stage required a microcalorimeter and fiber optics to guide the light [7–11,18–22]. The third stage would be the development of a UV-photocalorimeter that consists of a differential scanning calorimeter and an ultraviolet source, which is used extensively for the photostability evaluation of light-sensitive solid materials, including plastics [23–25], chemicals, and pharmaceuticals [9,10]; photopolymerization kinetics [26,27]; and characterization in vitrification and curing processes [28].

Much progress has been made to study in situ catalytic process, such as by using in situ Raman spectroscopy [29], in situ X-ray

* Corresponding author at: College of Chemistry and Chemical Engineering, Guangxi University for Nationalities, Nanning, 530006, China.

E-mail address: huangzaiyin@163.com (Z. Huang).

absorption techniques [30], and in situ infrared (IR) spectroscopy [31]. Nevertheless, in situ photocalorimetry offers an alternative method to study photocatalysis by tracing in situ thermodynamics and kinetics, which usually present a theoretical basis to analyze photocatalytic mechanisms [7]. In this work, a light-emitting diode (LED)-photocalorimeter was introduced that consists of a microcalorimeter and fiber optics to guide the light. The baseline of the LED-photocalorimeter can be adjusted to nearly zero by tuning the light intensity of two sources. After calibration by determining the photolytic enthalpy of potassium ferrioxalate, it was applied to trace the heat changes and kinetics in methylene blue (MB) photocatalysis over a visible-light-driven Ag@AgCl photocatalyst, combined with trapping experiments of active species and electron paramagnetic resonance (EPR) measurements, and the heat effects of the three stages and the stable exothermic rate of pollutant photodegradation were determined. The photocatalytic mechanisms were discussed in detail, thermodynamically, which demonstrates the application of the instrument in pollutant photodecomposition.

2. Experimental

2.1. Materials

Triethanolamine (>99.0%), isopropyl alcohol (>99.5%), p-benzoquinone (99%), potassium chloride (≥ 99.99), and D-(+)-glucose (AR) were purchased from Aladdin Reagent Ltd. (Southern California, USA) and used without further purification. Potassium ferrioxalate (>99.0%) was purchased from Shanghai Aijie Biological Technology Co. Ltd. (China). All other chemicals were analytical grade and used as purchased from Sinopharm Chemical Reagent Co. Ltd. without further purification. Pure water used in all experiments had a resistivity of $18.2\text{ M}\Omega\text{ cm}$ and was obtained from a Milli-Q system (Millipore).

2.2. Preparation of Ag@AgCl photocatalysts

Solvents composed of ethylene glycol and water (with a volume ratio of 5:1) were prepared in advance. Silver nitrate (AgNO_3 , 136 mg) was dissolved in 25 mL of 24 g L^{-1} polyvinyl pyrrolidone solution at room temperature, and stirred at 600 rpm in the dark for 10 min. Sodium chloride (NaCl , 5 mL of a 7 g L^{-1} solution) was injected rapidly into the aforementioned solution and precipitated for an hour. The solution gradually turned milky white, which indicates the formation of an AgCl precursor. One hour later, 5 mL of 18 g L^{-1} glucose solution was injected rapidly and was then kept in the dark for 3 h. Samples were separated by centrifugation, washed with a 1:1 volume ratio of water, ethanol and absolute ethanol, and then dried in a vacuum at room temperature.

2.3. Main active species detection during photocatalysis

Hydroxyl radicals ($\cdot\text{OH}$), the superoxide radical ($\text{O}_2^{\cdot-}$), and holes (h^+) were investigated by adding 1.5 mL of 1.0 mM IPA (a hydroxyl radical ($\cdot\text{OH}$) quencher), BQ (a superoxide radical ($\text{O}_2^{\cdot-}$) quencher), and TEOA (a hole (h^+) quencher) [32] to three tubes filled with 6 mL of 20 mg L^{-1} methylene blue aqueous solution and 9 mg of Ag@AgCl photocatalyst. The solutions were stirred at 600 rpm for 30 min in the dark and then irradiated in a XPA-7 photochemical reactor (Xujiang Electromechanical Plant, China) equipped with a 350 W Xe lamp. After a set interval, the irradiated solution was removed and its UV-vis spectrum was measured.

2.4. Electron paramagnetic resonance measurements

The active species in the photocatalysis of MB were trapped by a spin trap 5,5-dimethyl-1-pyrroline-N-oxide (DMPO) (Alfa-Aesar)

and detected by a Bruker A200 electron paramagnetic resonance spectrometer. The settings were a center field of 3480.0 G, a microwave frequency of 9.2–9.8 GHz, and a power of 20.0 mW. A solution containing 3 mg of Ag@AgCl, 1 mL of 20 mg L^{-1} MB, and $10\text{ }\mu\text{L}$ of DMPO was placed into a 15 mL glass tube and irradiated with 10 W LED light without stirring. EPR spectra were obtained before and after a predetermined irradiation time. A blank that contained only MB solution was also studied.

2.5. LED-photocalorimetry and its baseline adjustment to zero

A schematic illustration of the LED-photocalorimeter is shown in Fig. 1, which was designed by introducing LED light into an RD496L microcalorimeter (Mianyang Cp Thermal Analysis Instrument Co. Ltd., Mianyang, China) using optical fibers. Prior to using the LED-photocalorimeter, the microcalorimeter was calibrated by the Joule effect and its calorimetric constant was $(69.91 \pm 0.56)\text{ }\mu\text{V mW}^{-1}$ at 298.15 K. The dissolution enthalpy of KCl in deionized water ($1:1110, m_{\text{KCl}}/m_{\text{de-water}}$) was measured to be $(17.792 \pm 0.029)\text{ kJ mol}^{-1}$ (see the supporting information), which agreed well with the literature value of $(17.524 \pm 0.028)\text{ kJ mol}^{-1}$ [33], and thus indicates that the calorimetric system is accurate and reliable.

The LED-photocalorimeter works on a heat-conduction principle, in which the sample cell is surrounded by a heat-sink to maintain a constant temperature. Any heat variation is exchanged quantitatively with the heat-sink and the temperature change is detected using 649 pairs of thermopiles [8–10]. Based on the principle of differential calorimetry, the temperature difference between the sample and the reference is converted to a power signal, whose work principle is the same as that of differential scanning calorimetry, and this signal is magnified and recorded by a computer. Stainless steel cells are used throughout. The sample cell is charged with 1 mL of a mixture solution containing 1 mL of 20 mg L^{-1} MB and 3 mg of Ag@AgCl photocatalyst. The reference cell is charged with 1 mL of deionized water. The parameters are set up and the LED light is turned on after setting an equilibrium baseline at $25\text{ }^{\circ}\text{C}$. The heat effects in this process contain three main parts: (i) self-photodecomposition of MB, (ii) light-induced heat effects by incident light, and (iii) others derived from the photocatalysis of MB over photocatalysts. However, the heat effects, which are derived from (i) and (ii) are canceled out equally between the sample and reference cell. The recorded heat changes are therefore mainly derived from MB photocatalysis [7].

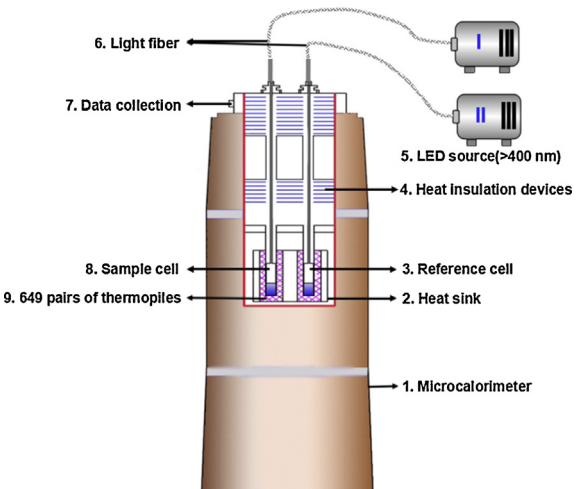


Fig. 1. Schematic illustration of LED-photocalorimeter.

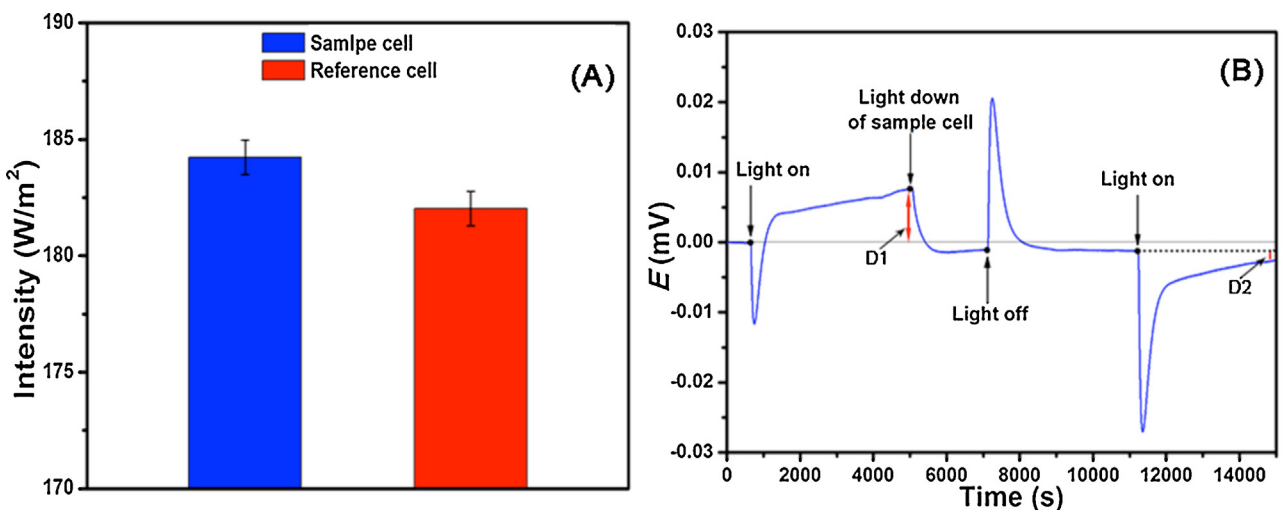


Fig. 2. Light intensity (A) of sample and reference cell and adjustment of baseline to zero by tuning the light intensity (B).

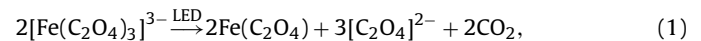
The main reason for choosing LED light as a source is that it is low cost, has a long lifetime, and is highly efficient with minimal energy burned off as heat [34]. LED lighting overcomes the shortcomings of Xe-arc lamps, which produce a significant amount of heat during irradiation. This heat masks the trace amounts of heat generated in the photoreaction, thereby making it extremely difficult to determine the photoreaction heat effects accurately [8]. The main wavelength of the LED sources lies between 400 and 650 nm (Fig. S2). The greatest challenge in the LED-photocalorimeter design is the adjustment of the baseline to zero. If the light intensity of two cells is unequal, the heat effects produced by the incident light would mask the trace amounts of heat generated in the photoreaction. Two existing methods are available to adjust the baseline to zero; a number of focusing and shuttering assemblies can be used [9–11] or the light source voltage can be controlled [22].

Three steps were taken for the adjustment. Firstly, the light intensity (Fig. 2A) of two optical fibers were adjusted roughly outside of the macrocalorimeter and determined 20 times using a solar power meter (TES-1333, TES Electrical Electronic Corp., Taiwan, China), which was $(184.23 \pm 0.75) \text{ W m}^{-2}$ for the sample cell and $(182.03 \pm 0.74) \text{ W m}^{-2}$ for the reference cell. Next, fine tuning of the light intensity was conducted after guiding LED light into the macrocalorimeter. As shown in Fig. 2B, despite the nearly close light intensity of the two optical fibers, its heat effects are not zero and its deviation (D1) is $7.786 \mu\text{V}$, which indicates that the light intensity of the sample cell is slightly larger than that of reference cell. To reduce the deviation from D1 ($7.786 \mu\text{V}$) to D2 ($1.461 \mu\text{V}$), the light intensity of the sample cell is reduced. It cannot be adjusted to zero since the LED light source cannot be more precisely tuned. Thirdly, to offset the baseline shift because of the trace heat deviation produced by the differential intensity of the two cells, a blank was used to record the heat changes generated by irradiation of the reference and sample cell charged with 2.0 mL deionized water under identical conditions. A subtraction of the photocatalysis heat flow from the blank eliminated any possible baseline shift and provided a more accurate calculation of heat change derived from the photocatalysis of MB over Ag@AgCl.

2.6. Calibration of LED-photocalorimeter

To demonstrate the rationality and reliability of the LED-photocalorimeter, potassium ferrioxalate was chosen as a target model. This reagent is used extensively as a chemical actinometer in the measurement of light intensity, because of its high sensitivity, ease of operation, affordability, and versatility over a wide

wavelength range [13,35–39]. When exposed to light with a wavelength of less than $\sim 490 \text{ nm}$, ferrioxalate ions undergo the following photodecomposition [36–39]:



The photolytic heat (Q) of the ferrioxalate at 25°C was measured using the LED-photocalorimeter and the concentration of Fe^{2+} ions was determined by measuring the absorbance after complexation with 1,10-phenanthroline ($\lambda_{\text{max}} = 510 \text{ nm}$). However, errors arise from the slow development times because the photooxidation of phenanthroline solutions may exceed 40%, depending on the age of the phenanthroline solution and the order of reagent addition [35]. Kirk et al. reported on a second potential error source where the excessive concentration of ferrioxalate slowed the color development, which suggests inhibition of $\text{Fe}(\text{phen})_3^{2+}$ complex formation [39]. Using the above recommendations [13,35–39], experiments were conducted with details provided in the supporting information.

3. Results and discussion

3.1. Characterization

Fig. 3B shows that the as-prepared Ag@AgCl is coral-like. It possesses a coral-like structure that is similar to porous materials, a size range from 20 nm to 200 nm, and a cross-sectional radius of $\sim (55.8 \pm 22.9) \text{ nm}$. The N_2 absorption–desorption isotherm (Fig. S3 in the supporting information) shows that the isotherms and hysteresis loops of Ag@AgCl belong to a typical type IV isotherm and type H3 loop (based on the IUPAC classification), which indicates the presence of no pores or macropores in its surface or large gaps between particles. The N_2 absorption–desorption isotherms as well as the corresponding pore distribution AgCl and P25 were also shown in Fig. S3 (in the supporting information).

The crystalline phase was investigated by X-ray powder diffraction (XRD). As shown in Fig. 3C, the XRD pattern of the as-prepared coral-like Ag@AgCl had a distinct diffraction peak at approximately $(2\theta) 27.7^\circ, 32.2^\circ, 46.2^\circ, 54.8^\circ, 57.5^\circ$, and 67.5° , which can be assigned to the $(111), (200), (220), (311), (222)$, and (400) crystal phases, respectively. These results agree with the diffractions of crystalline AgCl with a lattice constant $a = 5.549 \text{ \AA}$ (JCPDS file: 85-1355) [39]. The inset A is the amplification of the weak diffraction peak of Ag^0 at 38.2° , which is attributed to its trace amounts and poor crystallization. The XRD patterns of as-prepared AgCl are also

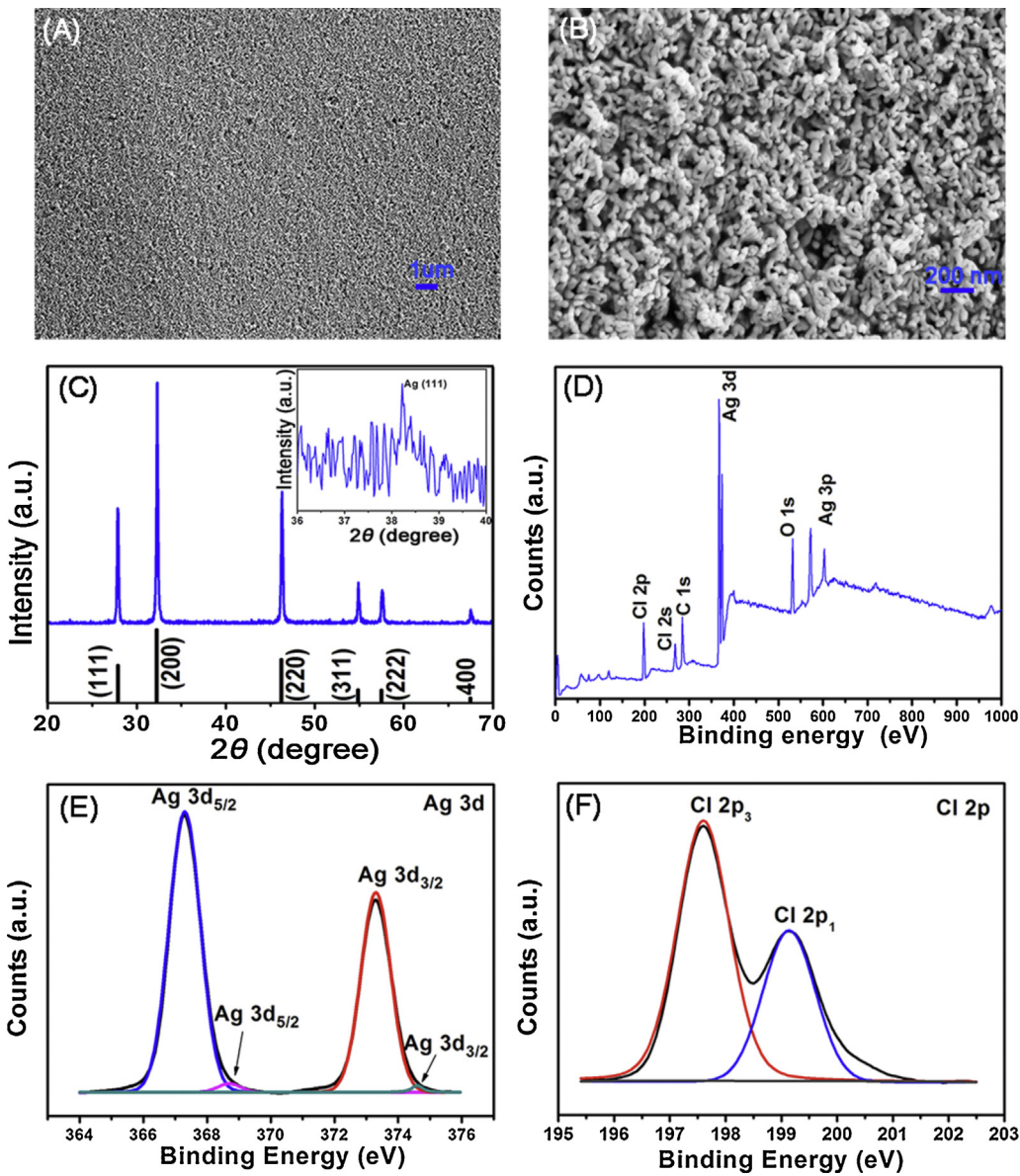


Fig. 3. Typical SEM images of as-prepared Ag@AgCl (A) and (B), XRD pattern of Ag@AgCl (C) and inset in (C): diffraction peak of Ag nanoparticles at 38.2° , XPS spectra of Ag@AgCl nanocomposites: survey spectrum (D), Cl 2p (E), and Ag 3d (F).

shown in Fig. S4 (in the supporting information), which agree with the diffractions of crystalline AgCl with a lattice constant $a = 5.549 \text{ \AA}$ (JCPDS file: 85-1355) [39]. SEM images of AgCl and XRD pattern of Ag@AgCl were presented in Fig. S4.

X-ray photoelectron spectroscopy (XPS) was used to study the elemental composition, chemical status, and Ag^0 content of the as-prepared Ag@AgCl. The trace amounts of C and O in the XPS spectrum (Fig. 3D) may be caused by adventitious hydrocarbon from the XPS instrument itself. The oxygen peak may be derived from oxygen adsorbed during Ag@AgCl preparation. Fig. 3E shows that the Ag 3d spectrum of the Ag@AgCl consists of two individual peaks at approximately 367.3 and 373.3 eV, which can be ascribed to binding energies of $\text{Ag } 3d_{5/2}$ and $\text{Ag } 3d_{3/2}$, respectively. The $\text{Ag } 3d_{5/2}$ and $\text{Ag } 3d_{3/2}$ peaks can be divided into two peaks at 367.3 and 368.7 eV and 373.3 and 374.6 eV, respectively, where the peaks at 367.3 and 373.3 eV are for the Ag^+ of AgCl [40], and those at 368.7 and 374.6 eV are attributed to metallic Ag^0 [40]. The surface ratio of the content of metallic Ag^0 and Ag^+ is 1:43.3, which explains why the diffraction peak of Ag^0 in the XRD pattern is so weak.

For Cl 2p (Fig. 3F), two peaks were obtained at binding energies of 197.7 and 199.3 eV, which correspond to $\text{Cl } 2p_{3/2}$ and $\text{Cl } 2p_{1/2}$ [40], respectively. Its content in the Ag@AgCl nanocomposites is 49.43%.

The UV-vis diffuse reflection of the photocatalysts is shown in Fig. 4A. Compared with P25 and AgCl, Ag@AgCl exhibits higher absorption coefficients in the broad visible regions, which is ascribed to the surface plasmon resonance (SPR) of the Ag nanoparticles deposited on the AgCl surface. In comparison with common AgCl with a large band gap (indirect band gap: 3.2 eV), the as-prepared Ag@AgCl with a smaller bandgap was found to be 2.69 eV (in Fig. S5), which demonstrates a significantly increased light absorption in the visible region ($\leq 461 \text{ nm}$). Its conduction and valence bands were calculated to be 0.225 and 2.915 eV, respectively (by the band-gap estimation shown in the supporting information).

Fig. 4B shows that the zeta potential of the Ag@AgCl and AgCl nanoparticles ranges from -15.23 to -30.30 mV when the pH changes from 5 to 7, whereas the zeta potential of P25 does not

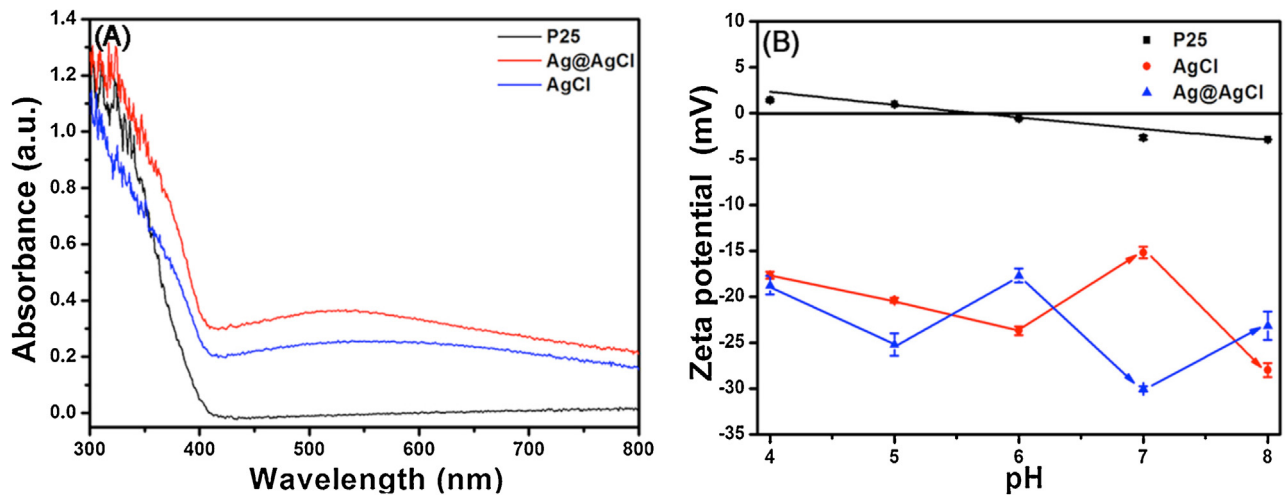


Fig. 4. (A) UV-vis diffuse reflection and (B) zeta potential of Ag@AgCl, AgCl, and P25, respectively.

change significantly. The Ag@AgCl, AgCl, and P25 particles are all nanosized, and form a type of colloidal solution when dispersed in aqueous solution. Because MB is a cationic dye, when mixed with a negatively charged photocatalyst, its interaction force cannot be ignored. This has a significant impact on absorption performance, and facilitates photocatalytic activity simultaneously.

3.2. Main active species of MB over Ag@AgCl

Because of similarities and the synergistic interaction of semiconduction and localized SPR (LSPR), hybrid nanostructures composed of semiconductors and noble metals (i.e. Ag, Au, Pt) have been receiving extensive attention [41,42]. The Ag@AgCl plasmonic photocatalyst [43–45] was therefore chosen in this work.

Fig. 5A displays curves of the degradation rate of MB versus irradiation time for the trapping experiments by the addition of 1 mM IPA, BQ, and TEOA. The photocatalytic degradation of MB decreased visibly with IPA addition. After photocatalysis for 30 min, the degradation rate with IPA, BQ, and TEOA addition was 14.47, 60.88, and 22.45%, respectively. Compared with 75.6% of the blank in 30 min, therefore, it can be concluded that the main active species change as $\bullet\text{OH} > \text{h}^+ > \text{O}_2\text{'}^-$.

Fig. 5B shows the EPR spectra obtained before and after 10 min of LED irradiation of DMPO + MB and DMPO + Ag@AgCl + MB suspensions. The peak locations and characteristic 1:2:2:1 relative peak magnitudes (marked by blank boxes in Fig. 5B) are attributed to trapped hydroxyl radicals in the form of DMPO-OH [46]. Compared with MB solution, after 10 min of irradiation, the presence of Ag@AgCl photocatalysts facilitates the generation of hydroxyl radicals per unit time. The peak locations marked by blank circles in Fig. 5B may be caused by DMPO self-decomposition, whose decomposed products increase with increasing irradiation time and result in high peak magnitudes. Meanwhile, the blank that contains only MB solution also shows the presence of trapped hydroxyl radicals after 10 min of irradiation, which indicates that electrons are generated by self-sensitized MB under visible light.

Fig. 6 shows the photoresponse mechanism scheme of the Ag@AgCl photocatalyst under visible light irradiation. Ag and AgCl can be excited by visible light. Because of the SPR and the dipolar character of metallic Ag, hole-electron pairs were produced [31]. Based on the UV-vis absorption spectra of Ag@AgCl, hole-electron pairs can also be generated because of their small band gap (2.69 eV). Subsequently, free electrons produced by Ag nanoclusters would flow preferentially to the n-type AgCl semiconductor because of the different work function [43,47] ($\Phi_{\text{Ag}} = 4.26 \text{ eV}$,

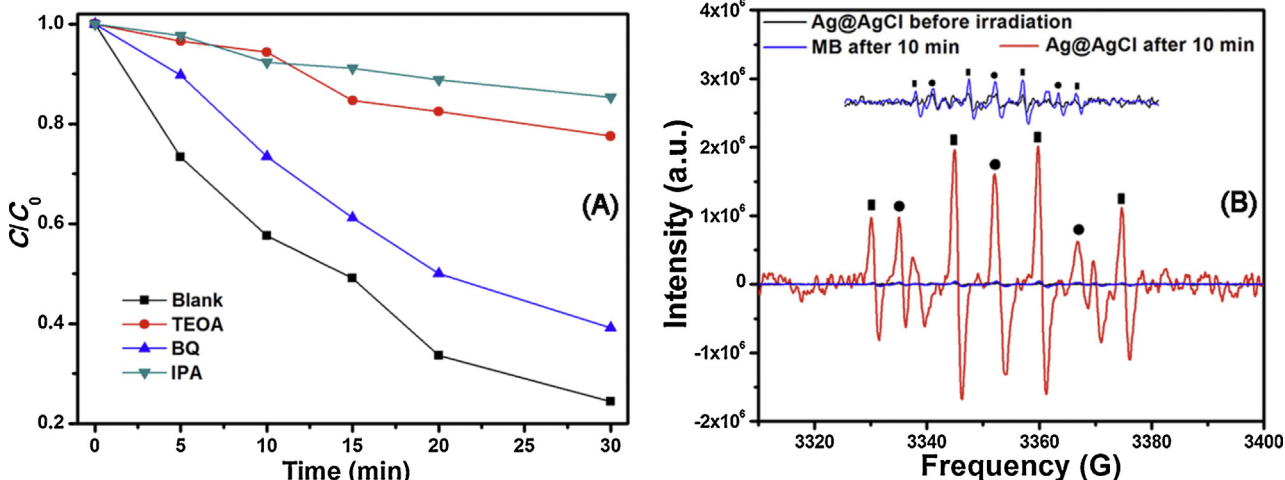


Fig. 5. (A) Trapping experiments after 30 min of irradiation under 300 W Xe lamp and (B) EPR spectra for DMPO-containing Ag@AgCl suspension before and after 10 min of irradiation and MB solution after 10 min of irradiation. The inset is the enlarged image of MB after 10 min of irradiation and Ag@AgCl before irradiation.

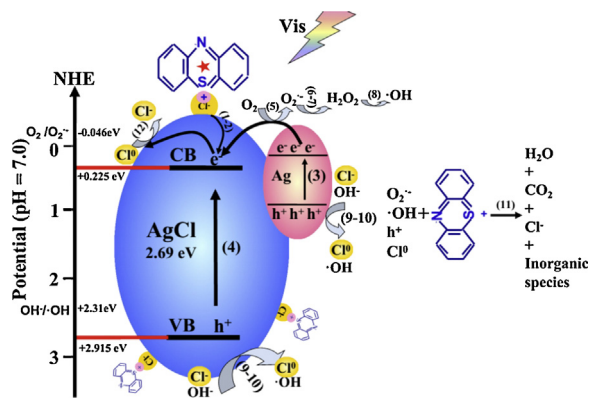
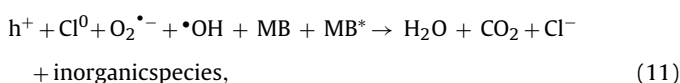
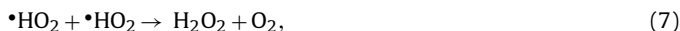
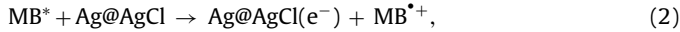


Fig. 6. Photocatalytic mechanism scheme of MB over Ag@AgCl under visible light.

$\Phi_{\text{AgCl}} = 6.3 \text{ eV}$ [48]. After the formation of an equilibrated Fermi level between the semiconductor AgCl and Ag NPs, a Schottky barrier would be formed at their junction interface [45–49], which can facilitate photo-induced carrier separation. The electrons generated by sensitized MB also transform to CB (conduction band). However, the electrons on the CB of AgCl (0.225 eV vs. NHE) could not reduce O_2 to $\text{O}_2^{\bullet-}$ since its CB potential is more positive than $E_0(\text{O}_2^{\bullet-}/\text{O}_2^-)$ (−0.046 eV vs. NHE) [31,43]. As described in Eqs. (5)–(8), the partial electrons transform from Ag NPs to AgCl and combine with dissolved oxygen in water, followed by the formation of $\bullet\text{OH}$ [39]. The weak acidic MB solution (pH of ~6.10) favors the formation of $\text{O}_2^{\bullet-}$, and facilitates the production of $\bullet\text{OH}$ species. Holes in the Ag NPs are restricted. These diffuse gradually to its surface [45], and finally unite Cl^- and OH^- to form Cl^0 and $\bullet\text{OH}$. The holes in the VB (valence band) of AgCl (+2.915 eV vs. NHE) can reduce Cl^- and OH^- to Cl^0 and $\bullet\text{OH}$ [50]. The Cl life cycle is as follows: Cl^- is oxidized by holes during photocatalysis [39,43,49] and Cl^0 reduction occurs when it reacts with electrons in the CB of AgCl and decomposes pollutants [31].



3.3. Heat flow curves of photolysis of potassium ferrioxalate and its photolytic enthalpies.

Fig. 7 displays heat flow curves of photolysis of potassium ferrioxalate under different irradiation time of LED light. In order to offset the baseline shift derived from trace heat deviation produced by the differential intensity of two cells, the blank was conducted under identical conditions by recording the heat changes of reference and sample cell both charged with 2.0 mL of deionized water, net reaction was the subtraction of heat flow of photolysis from the blank, which eliminated any possible baseline shift and gave an more accurate calculation of heat changes resulting from the photolysis of potassium ferrioxalate. As shown in Fig. 7A, the blank went through weak exothermic stage and finally recovered from a endothermic peak when the light was turn off, its heat changes (integrated area of the heat flow curve of the blank) was almost offset and near to zero; While heat changes of net reaction went through an endothermic stage and then recovered to a stable exothermic stage, namely, the net reaction occurred a initial photoresponse of potassium ferrioxalate and then the balance between endothermic photoresponse and heat release from its photolysis.

The photolytic heats (Q) of potassium ferrioxalate under different irradiation time at 25°C were calculated by integrating area of heat flow curve of net reaction in Fig. 7. And UV-vis absorption of the complexation is displayed in Fig. S6 (in the supporting information). As shown in Table 1, the standard molar reaction enthalpy of the photolysis of ferrioxalate determined was (-57.7316 ± 3.062) kJ mol $^{-1}$, which is close to (-53.5808 ± 2.9300) kJ mol $^{-1}$ in the literature [13], and indicates that the instrument is reasonable and reliable.

3.4. Heat flow curves of methylene blue photodegradation over Ag@AgCl

One of the shortcomings of the LED-photocalorimeter is that the reaction cell cannot be stirred because of design challenges. During photocatalysis, incident light was primarily absorbed and scattered by photocatalyst colloid nanoparticles, which resulted in a limited optical path (denoted by d in Fig. S7 in the supporting information) [7,8]. According to the dynamic properties of colloid particles, nanoparticles precipitate and move downward by the force of gravity. Brownian motion provides an opposite driving force, increases the distance between nanoparticles, and stabilizes its concentration. When the two opposite forces are balanced, the downward precipitation rate is extremely slow and a particle concentration gradient forms in the vertical direction, which is more dense when it is much closer to the bottom. This results in a higher absorption and scattering of incident light with a vertical attenuation of its intensity, which finally disappears at the interface (denoted by b in Fig. S7 in the supporting information).

Three main heat changes occurred during the photodegradation of MB over Ag@AgCl: (a) photoresponse of methylene blue molecules and photocatalyst, (b) the balance between endothermic

Table 1

Table 1
Standard molar reaction enthalpies of photolysis of potassium ferrioxalate at 25 °C.

Irradiation time (min)	Ferrous complex absorbance (A_f)	Reference absorbance (A)	Difference absorbance (ΔA)	Molar of produced Fe^{2+} (mol)	Q (J)	Enthalpies ($\Delta_r H_m^\theta$ kJ mol $^{-1}$)
15	1.9579	0.0119	1.9460	3.5125×10^{-6}	0.2054	-58.4878
15	2.0253	0.0119	2.0134	3.6342×10^{-6}	0.2244	-61.7442
25	3.0716	0.0119	3.0597	5.5228×10^{-6}	0.3068	-55.5519
25	3.0270	0.0119	3.0151	5.4423×10^{-6}	0.3001	-55.1426
Average						-57.7316 ± 3.062

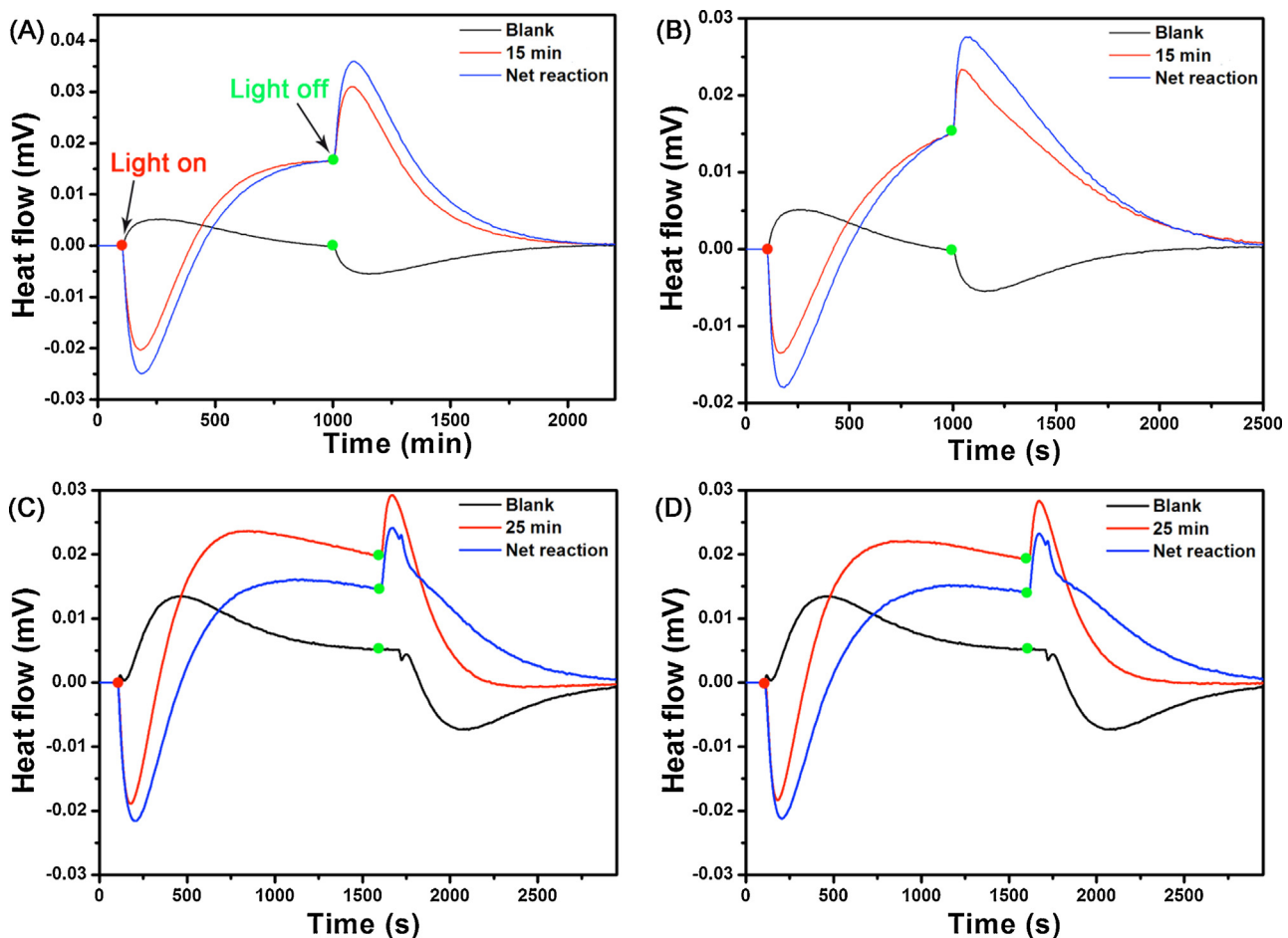


Fig. 7. Heat flow curves of photolysis of potassium ferrioxalate under different irradiation time of LED light: (A) and (B) in 15 min, (C) and (D) in 25 min.

photoresponse and the pollutant photodegradation, and (c) stable exothermic period of pollutant photodegradation.

To offset the baseline shift derived from the trace heat deviation produced by the differential intensity of the two cells, a blank test was conducted under identical conditions. As shown in Fig. 8A, the heat changes generated by irradiation of the reference and sample cells that were charged with 2.0 mL of deionized water, indicate that the net reaction was a subtraction of photocatalysis heat flow from the blank, which eliminated any possible baseline shift and gave a more accurate calculation of heat change that results from the photocatalysis of MB over Ag@AgCl.

As shown in Fig. 8A, stage ab in the net reaction is endothermic with a heat value of +73.8 mJ (integrated area of the heat flow curve of ab), which is attributed to the photoresponse of Ag@AgCl to incident LED light. (I) The production of electron-hole pairs from the LSPR of the Ag NPs is driven by visible light and the formation of active species. (II) MB self-decomposition, in order to confirm how many heat effects are derived from MB self-decomposition, the blank was conducted with the reference and sample cells charged with 1.0 mL of deionized water and 1.0 mL of 20 mg L⁻¹ methylene blue aqueous solution, respectively. Offsetting the baseline shift, heat flow curves of MB self-decomposition were shown in Fig. 8B, it went through an initial endothermic peak in response to incident light and the balance between endothermic photoresponse and the MB self-decomposition, and finally a stable exothermic stage. The heat effects derived from MB self-decomposition (integrated area of abe in Fig. 8B) account for 69.1% of that in photocatalysis of MB over Ag@AgCl (integrated area of abf in Fig. 8B). In the presence photocatalyst, it simultaneously

occurred self-decomposition of MB and photodecomposition of MB degraded by active species, while the reactivity of the two decompositions is different with time continuing. In the beginning of photocatalysis, MB molecules and photocatalyst nanoparticles were induced by visible light; MB molecules mainly undergo self-decomposition with an endothermic process during photocatalyst in response to incident light (III). Active species are adsorbed on the photocatalyst surface and intermediate products of MB escape from the interaction of strong surface forces and diffuse into the MB solution. This is a weak endothermic process and increases with continuing reaction (VI). The slow precipitation of nanoparticles converts gravitational potential energy to kinetic energy, and is accompanied by the mass transfer of MB molecules on the photocatalyst surface. The heat effect is ignored because it is a balance between adsorption and desorption.

The bc stage (Fig. 8) with a heat value of +143.9 mJ (integrated area of the heat flow curve of bc) is the balance between the endothermic photoresponse and the photodegradation of pollutants. As the reaction continues, the concentration of active species increases gradually and photodecomposition of MB gradually predominates. The heat is released from the photooxidation of MB, and the number of its intermediate products also increases, which results in a decrease in the endothermic peak. The system finally enters an exothermic stage.

When irradiated in 3080 s (denoted by c), the heat flow curve in Fig. 8 finally reaches a maximum exothermic value and maintains a stable exothermic rate of $-(0.1543 \pm 0.0446) \text{ mJ s}^{-1}$. It is important to note that the interface b of the optical path moves slowly downward with the precipitation of photocatalytic nanoparticles;

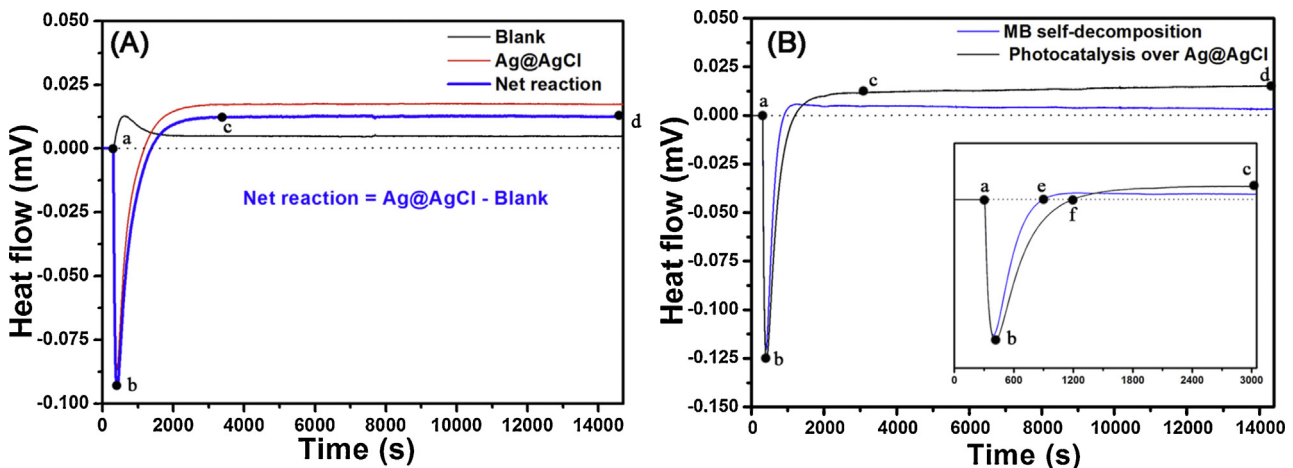


Fig. 8. Heat flow curves (A) of photocatalysis of MB over Ag@AgCl, blank (irradiation of reference and sample cell charged with 2.0 mL deionized water under identical conditions), and net reaction (subtraction of heat flow of photocatalysis from the blank); heat flow curves (B) of photocatalysis of MB over Ag@AgCl and MB self-decomposition (0–14,400 s), the inset: the enlarged heat flow curves (0–3000 s).

the downward speed of motion of interface b is controlled directly by the precipitation rate. Therefore, for these nanoparticles to reach a sedimentation equilibrium in the optical path, the number of activated photocatalysts must be kept constant. This results in a certain amount of active species generated per unit time, which determines directly the exothermic rate and provides a stable organic photooxidation rate per unit time. This stage also contains weak heat effects of the photocatalyst photoresponse, the self-decomposition of MB, and the mass transfer. In conclusion, the exothermic platform (cd) is derived mainly from the photooxidation of organics. Even if the solution is irradiated for 4 h, the heat flow curve would not return to the baseline because of incomplete photodegradation of organics (the corresponding residual MB is at least 17.4%, Fig. 9B). After irradiation for 4 h, the entire photocatalysis heat effect is -1721.5 mJ .

3.5. Thermokinetics during photocatalysis of MB over Ag@AgCl photocatalyst

The reaction heat liberated during photocatalysis is directly proportional to the concentration of MB molecules reacted in the system. By integrating the area under the exothermic peak of the

net reaction in Fig. 8, the decomposition rate of MB or the extent of reaction (ξ) can be defined according to Eq. (13):

$$\xi = \frac{\Delta Q_t}{\Delta Q_0^{\text{theor}}}, \quad (13)$$

where ΔQ_t is the reaction heat released at time t and $\Delta Q_0^{\text{theor}}$ is the theoretical heat for complete photodecomposition of MB over a photocatalyst. The rate of photocatalysis (R_t) is related directly to the rate of heat changes (dQ/dt) by the following:

$$R_t = \frac{d\xi}{dt} = \frac{(dQ_t/dt)}{\Delta Q_0^{\text{theor}}}, \quad (14)$$

Fig. 9A shows the rate of heat change released from the photocatalysis of MB using Ag@AgCl as a photocatalyst in real time. Stage ac is the photoresponse of Ag@AgCl to LED light. The stable exothermic rate of photodegradation of MB in stage cd is $-(0.1542 \pm 0.0446) \text{ mJ/s}$, which shows that the reaction in cd is pseudo-zero-order. Gaisford et al. demonstrated that photocalorimetry is generally applicable to zero-order processes in the photodegradation of nifedipine, and reported that under a constant light power, the number of molecules of nifedipine reacting per unit time must be the same, irrespective of the volume used [11].

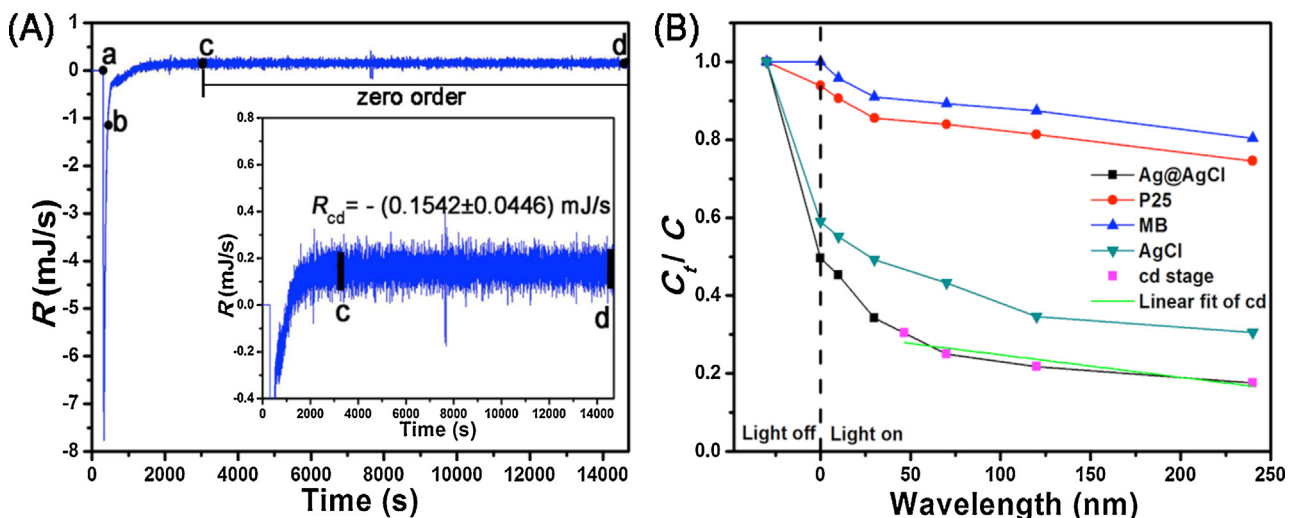


Fig. 9. (A) Rate of photocatalysis of MB in the net reaction. Inset: magnification of cd stage. (B) Photocatalytic dynamic curves for degradation of MB over commercial P25, AgCl, and Ag@AgCl.

For the rate of photocatalysis in the cd stage (Fig. 9A), the number of activated photocatalysts in the light path are constant. This results in a certain amount of active species generated per unit time, which determines the exothermic rate and provides a pseudo-zero-order process. These results agree with those from the UV-vis spectra (Fig. 9B), which indicates that the cd stage of net reaction is a pseudo-zero-order process.

Photocatalytic dynamic curves for degradation of MB over commercial P25, AgCl, and Ag@AgCl are also obtained under identical conditions by the determination of UV-vis spectra of the MB solution after irradiation for different times (Fig. 9B). Prior to irradiation, the high capability of absorption over Ag@AgCl is attributed to a strong electrostatic attraction between negatively charged Ag@AgCl colloids and a cationic MB molecule. After irradiation for 4 h, the photodegradation rate of MB over Ag@AgCl is up to 82.6% without complete decomposition for the slow downward motion of photocatalytic nanoparticles in the light path. The number of excited photocatalyst nanoparticles is low and many nanoparticles are inactive at the bottom without light irradiation. This is a result of the photocalorimeter not containing a stirring apparatus. We hope to offer an alternative method to study the *in situ* photocatalysis. A novel photocalorimeter–fluorescence/Raman spectrum combined system is being processed, which combines the advantage of both photocalorimeter and *in situ* spectra technology, and equipped with a monochromatic light source, a bubbling device, and fluorescence/Raman spectrometry. The combined system will be more versatile and able to obtain multi-dimensional information during the photoreaction, including thermodynamic information, kinetics, and spectroscopy information on the intermediate products.

4. Conclusions

An alternative method to study photocatalysis thermodynamically by tracing its thermodynamics and kinetics in real-time using an *in situ* LED-photocalorimeter was introduced. The baseline of the LED-photocalorimeter can be adjusted to nearly zero by tuning the light intensity of the two sources. After its calibration by determining the photolytic enthalpy of potassium ferrioxalate, we applied it for the first time to trace the heat changes and thermokinetics in the photocatalysis of MB over a visible-light-driven Ag@AgCl photocatalyst. Three main heat changes occurred: (i) photoresponse of methylene blue molecules and photocatalyst, (ii) balance between endothermic photoresponse and pollutant photodegradation, and (iii) stable exothermic stage in pollutant photodegradation. An initial endothermic reaction and then an exothermic stage occurred. A final stable exothermic rate was maintained which is $-(0.1543 \pm 0.0446) \text{ mJ s}^{-1}$ and is a pseudo-zero-order process. The heat effects of stages (i), (ii), and (iii) are 73.8, 143.9, and -1939.2 mJ , respectively. The photocatalytic mechanisms were discussed in detail, thermodynamically, which demonstrates the application of the instrument in pollutant photodecomposition. Thus it is believed that the photocalorimeter and photocalorimeter–fluorescence/Raman spectrum combined system will be of paramount significance for promising applications to investigate *in situ* photochemistry, physics, and biomedicine.

Conflict of Interest

The authors declare no competing financial interest.

Acknowledgements

Thanks for the financial support from the Natural Science Foundation of China (20963001, 21273050). We would express our great appreciation to Prof. Kaibin Tang for the determination of X-ray photoelectron spectroscopy (University of Science and

Technology of China), Prof. Aiwen Lei for providing access to EPR measurement (Wuhan University), Prof. Min Zhang in photoreaction experiment of potassium ferrioxalate (Guangxi University), and Guangxi Colleges and Universities Key Laboratory of Food Safety and Pharmaceutical Analytical Chemistry (Guangxi University for Nationalities).

Appendix A. Supplementary data

Supplementary data associated with this article can be found, in the online version, at <http://dx.doi.org/10.1016/j.apcatb.2015.07.036>.

References

- [1] A. Fujishima, K. Honda, *Nature* 238 (1972) 37.
- [2] H. Takashi, K. Jun, D. Kazunari, *Chem. Soc. Rev.* 43 (2014) 7520.
- [3] T.P. Michael, A.R. Danica, B.C. David, *Science* 339 (2013) 1593.
- [4] M.N. Chong, B. Jin, C.W.K. Chow, C. Saint, *Water Res.* 44 (2010) 2997.
- [5] C.C. Chen, W.H. Ma, J.C. Zhao, *Chem. Soc. Rev.* 39 (2010) 4206.
- [6] X.H. Bao, *Sci. China Ser. B-Chem.* 10 (2009) 1125.
- [7] X.X. Li, G.C. Fan, Z. Ma, X.C. Tang, Z.Y. Huang, *Sci. China Ser. B-Chem.* 10 (2014) 1576.
- [8] X.X. Li, Z.Y. Huang, G.C. Fan, Y.N. Wu, X.C. Tan, *Chem. J. Chinese U.-Chinese 7* (2014) 1480.
- [9] M. Dhuna, A.E. Beezer, A.C. Morris, *Rev. Sci. Instrum.* 78 (2007) 1.
- [10] M. Dhuna, A.E. Beezer, J.A. Connor, *J. Pharm. Biomed. Anal.* 48 (2008) 1316.
- [11] L.A. Sousa, A.E. Beezer, L.D. Hansen, D. Clapham, J.A. Connor, S. Gaisford, *J. Phys. Chem. B* 116 (2012) 6356.
- [12] J.L. Magee, T.W. Dewitt, E.C. Smith, F. Daniels, *J. Am. Chem. Soc.* (1939) 3529.
- [13] A.W. Adamson, A. Vogler, *Hican, J. Am. Chem. Soc.* 100 (1978) 1298.
- [14] J. Olmsted III, *Rev. Sci. Instrum.* 50 (1979) 1256.
- [15] J. Olmsted III, *J. Am. Chem. Soc.* 102 (1980) 66.
- [16] M. Nakashima, A.W. Adamson, *J. Phys. Chem.* 86 (1982) 2910.
- [17] Y. Harel, A.W. Adamson, *J. Phys. Chem.* 91 (1987) 901.
- [18] B. Scharschmidt, I. Lamprecht, *Specalia* 4 (1973) 505.
- [19] A. Cooper, C.A. Converse, *Biochemistry* 15 (1976) 2970.
- [20] A. Cooper, *Nature* 282 (1979) 531.
- [21] R.R. Birge, T.M. Cooper, A.F. Lawrence, M.B. Masthay, C. Vasilakis, C.F. Zhang, R. Zidovetzki, *J. Am. Chem. Soc.* 111 (1989) 4063.
- [22] V.S. Mukhanov, R.B. Kemp, *J. Therm. Anal. Calorim.* 3 (2009) 3731.
- [23] C.E. Corcione, R. Striani, M. Frigione, *Prog. Org. Coat.* 6 (2014) 1117.
- [24] Y.H.X.Z. Li, S. Sun, *J. Am. Oil Chem. Soc.* 8 (2014) 1425.
- [25] K.S. Anseth, R.A. Scott, N.A. Peppas, *Macromolecules* 29 (1996) 8308.
- [26] S.H. Dickens, J.W. Stansbury, K.M. Choi, C.J.E. Floyd, *Macromolecules* 36 (2003) 6043.
- [27] J. Wei, F. Liu, *Macromolecules* 42 (2009) 5486.
- [28] C.A.G. Fernandez, P. Davies, S. Gomez-Barreiro, J.L. Beceiro, *J. Therm. Anal. Calorim.* 102 (2010) 1057.
- [29] F.T. Fan, Z.C. Feng, C. Li, *Acc. Chem. Res.* 3 (2010) 378.
- [30] S. Bordiga, E. Groppo, G. Agostini, J.A.V. Bokhoven, C. Lamberti, *Chem. Rev.* 113 (2013) 1736.
- [31] D.G. Gong, V.P. Subramaniam, J.G. Highfield, Y.X. Tang, Y.K. Lai, Z. Chen, *ACS Catal.* 1 (2011) 864.
- [32] L.Q. Ye, J.Y. Liu, C.Q. Gong, L.H. Tian, T.Y. Peng, L. Zan, *ACS Catal.* 2 (2012) 1677.
- [33] R. Rychly, V.J. Pekárek, *J. Chem. Thermodyn.* 9 (1977) 391.
- [34] S. Dominguez, P. Ribao, M.J. Rivero, I. Ortiz, *Appl. Catal. B Environ.* 178 (2015) 165.
- [35] W.D. Bowman, J.N. Demas, *J. Phys. Chem.* 21 (1976) 2434.
- [36] A.D. Kirk, C. Namasivayam, *Anal. Chem.* 55 (1983) 2428.
- [37] Y. Quan, S.O. Pehkonen, M.B. Ray, *Ind. Eng. Chem. Res.* 43 (2004) 948.
- [38] J.S. Lee, J.W. Kim, W.Y. Choi, *Environ. Sci. Technol.* 41 (2007) 5433.
- [39] H.J. Kuhn, S.E. Braslavsky, R. Schmidt, *Pure Appl. Chem.* 76 (2004) 2105.
- [40] Y.H. Ao, H. Tang, P.F. Wang, C. Wang, *Mater. Lett.* 131 (2014) 74.
- [41] C.H. An, J.Z. Wang, W. Jiang, M.Y. Zhang, X.J. Ming, S.T. Wang, Q.H. Zhang, *Nanoscale* 4 (2012) 5646.
- [42] X.M. Zhou, G. Liu, J.G. Yu, *J. Mater. Chem.* 22 (2012) 21337.
- [43] R.B. Jiang, B.X. Li, C.H. Fang, J.F. Wang, *Adv. Mater.* 31 (2014) 5274.
- [44] P. Wang, B.B. Huang, X. Qin, X.Y. Qin, X.Y. Zhang, Y. Dai, *Angew. Chem. Int. Ed.* 47 (2008) 7931.
- [45] X.C. Ma, Y. Dai, J.B. Lu, M. Guo, B.B. Huang, *J. Phys. Chem. C* 116 (2012) 19372.
- [46] T. Uchino, H. Tokunaga, M. Ando, H. Utsumi, *Toxicol. In Vitro* 16 (2002) 629–635; H.Y. Li, T.S. Wu, B. Cai, W.G. Ma, Y.J. Sun, S.Y. Gan, D.X. Han, L. Niu, *Appl. Catal. B Environ.* 164 (2015) 344.
- [47] C. Clavero, *Nature Photonics* 8 (2014) 95.
- [48] P. Wang, B.B. Huang, Y. Dai, M.H. Whangbo, *Phys. Chem. Chem. Phys.* 14 (2012) 9813.
- [49] B.W. Ma, J.F. Guo, W.L. Dai, K.N. Fan, *Appl. Catal. B Environ.* 130–131 (2013) 257.
- [50] G.V. Buxton, C.L. Greenstock, W.P. Helman, A.B. Ross, W.J. Tsang, *J. Phys. Chem. Ref. Data* 456 (17) (1988) 513.